Scattering of surface-plasmon polaritons by dipoles near a surface: Optical near-field localization

Mufei Xiao*
Laboratorio de Ensenada, Instituto de Física, Universidad Nacional Autonoma de México, Apartado Postal 2681, Codigo Postal 22800 Ensenada, Baja California, Mexico and Nanchang Institute of Aeronautical Technology, 330034 Nanchang, China

Anatoly Zayats
Unidade de Ciencias Exactas e Humanas, Universidade do Algarve, 8000 Faro, Portugal

Jesús Siqueiros
Laboratorio de Ensenada, Instituto de Física, Universidad Nacional Autonoma de México, Apartado Postal 2681, Codigo Postal 22800 Ensenada, Baja California, Mexico and Centro de Investigación Científica y de Educación Superior de Ensenada, Apartado Postal 2732, Codigo Postal 22800 Ensenada, Baja California, Mexico

(Received 5 August 1996)

Electromagnetic radiation of electric dipoles, which are placed near a metallic surface and excited by the ongoing surface polaritons, is investigated. The dipoles are used to represent the surface scattering centers, irregulars, and mesoscopic particles. A formalism which distinguishes the evanescent field and propagating waves in the dipole radiation is employed to calculate the scattered surface polariton field in the near- and far-field zones. Numerical studies of the local field at the dipole sites were carried out for 50 dipoles with various distances between the dipoles and between the dipoles and the surface. An enhanced local field was obtained in some cases, and the conditions for the enhancement are discussed. Two-dimensional intensity distributions of the scattered field in the plane perpendicular to the surface and in the plane parallel to the surface for systems with up to 100 dipoles are presented for the propagating waves, the evanescent field, and the total field. Finally, a scanning local probe is introduced in the self-consistent calculations, and a numerical modeling of the near-field optical microscopy over the dipole system excited by the surface polaritons is carried out for various tip-surface separations. The results are employed to discuss phenomena in the surface polariton optics, particularly the recently observed strong optical near-field localization. [S0163-1829(97)01404-5]

I. INTRODUCTION

A surface polariton (SP) is a mode under which an electromagnetic wave propagates along the surface. The behavior of surface polaritons at rough surfaces has been under intensive investigation since the last decade.[1,2] The electromagnetic field associated with SP's is concentrated in the interface region and, thus, is very sensitive to defect structure and surface roughness.[2–4] The lateral distribution of a SP field over a surface depends strongly on the surface roughness. Scattering of SP's by the surface roughness leads partially to radiation in the vacuum half-space, and partially to the recreation of SP's on the surface. The strength of a surface polariton field is determined not only by surface inhomogeneity but also by the SP field enhancement at the defects. Therefore, variation of the SP field across the surface reflects the defect distribution as well as the defect sizes and the local dielectric parameters. In spite of numerous theoretical studies, until now there has not been a full understanding of these phenomena to our knowledge.

Experimentally the scattering of SP's has been studied for a long time in the far-field domain,[3,4] where only the far-field radiation in the vacuum is measured and the subwavelength information concerning the individual mesoscopic scatterers is lost. The recent development of near-field scanning optical microscopy (NSOM) (Refs. 5–9) opens the possibility of measuring an optical near field close to the sample surface. In NSOM, a local probe of size smaller than the light wavelength is placed adjacent to the sample surface within a range shorter than the light wavelength. Resolutions beyond the Rayleigh criterion[10] ($\sim\lambda/2$, λ being the light wavelength) have been achieved in NSOM with various configurations.[6,9,11–18] A common understanding of this super-resolution is that the near-field detection retrieves the evanescent field which is stationary around the scattering source. The evanescent field is the inhomogeneous part in the total radiation, which is an exception from the classic diffraction.

Naturally, one is interested in combining the aforementioned two domains: the near-field detection and the surface polariton scattering. Experiments have been reported in perturbation of a surface-plasmon polariton by using a metallic tip in the near-field region,[18,19] and in the characterization of the polariton (such as the propagation and decaying length of a SP) with a near-field optical microscope.[20,21]

Direct observation, using a near-field scanning optical microscope, of the scattering of surface polaritons on a rough metallic surface excited with total internal reflection technique has been recently performed.[22–25] In Refs. 22 and 23, highly localized light dots on a gold surface were observed

with a near-field optical microscope. It was experimentally demonstrated that the observed optical near-field images do not coincide with the topographic relief obtained simultaneously by a shear force microscope. Thus the localized near-field light dots take place in the area where, not necessarily, there are similar surface irregulars. The NSOM technique was also used by Tsai *et al.*[24] in similar experiments to observe light localization on silver fractal clusters. They attempted to explain the observed data by computational studies which take into account the dipole-dipole interactions between the large-scale fractal clusters. The collective resonant effects were found to be responsible for the light localization. Recently, Krenn *et al.*[25] performed photon scanning tunneling microscopy on discrete nanometric silver particles. A localized near field was observed, and plasmon excitation in the individual particles with various shapes and sizes was believed to be the main cause.

In parallel, for recent times, theoreticians have been trying to offer a fair theoretical explanation for the localization of electromagnetic field.[26–30] Many studied, as already mentioned, the optical coupling among a large group of particles on surface (see Refs. 24 and 26 and the references therein). Others studied continued random rough surfaces[27] by looking for, in angular spectrum representation, plane-wave modes resonantly fit to the roughness. A number of theories have been developed for surface-enhanced scattering,[28–30] in which some useful numerical methods have been applied successfully to explain various surface-enhanced scattering phenomena. The anomalous scattering is, to some extent, related to the disorder of the surface roughness. Based on such a point of view, various numerical simulations have been reported, some of which did provide fair agreement with the experimental results (see, e.g., a review in Ref. 28).

Microscopically, multiradiation between the scattering centers seems the cause of the field localization.[28] Part of the incident light is multiply scattered by more than one scattering centers before going out of the surface, while another part of the incident light may travel along the same path but in an opposite direction. The interference between these two waves results in an enhancement in the far-field radiation. The enhanced radiation in the far field is sometimes referred to as the weak localization. If the scattering path is a closed loop, the light cannot escape, which is called strong localization. In analogy to electron localization,[31] in the latter case one is able to define a diffusion length and consider the localization as a case of zero diffusion.

In the present paper, we deal with so-called optical near-field localization. The surface roughnesses that we are interested in are the subwavelength structures on the surface. The distances between the scattering centers are assumed to be so small that the multiradiation of the propagating waves would be less than or equally important to comparing with the evanescent coupling between the scatterers. Our model is a system containing a group of mesoscopic spheres distributed near a surface. These small spheres are labeled by their dipole polarizability. Assuming a surface wave traveling across the spheres, we calculate self-consistently the local field at the sites of the spheres.[32–35] The field distribution in the half-space can then be calculated by summing up the dipole radiation from each sphere. A formalism which distinguishes the propagating wave and the evanescent field is employed to calculate separate field distributions for the propagating, evanescent, and total field.[36–38] In Sec. IV we present, for various arrangements of the spheres, the field intensity distribution in the x-z plane (perpendicular to the surface) and in the x-y plane (parallel to the surface). We clearly show the separate propagating and evanescent field distributions and their importance for localization processes. Finally, the influence of the local probe on the field distribution is studied with a self-consistent model calculation that takes into account the presence of the probe tip. We also discuss the imaging quality and the resolution of the near-field scanning optical microscope working for surface polariton detection.

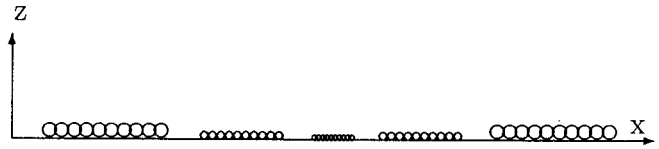

FIG. 1. Scheme of a system of 50 silver spheres placed on top of a silver surface. For all spheres, y coordinates are zero, z coordinates are a, and the center-center separation between two neighboring spheres is $2a$, where a is the radius of the sphere: from left to right, for spheres 1–10 $a=100$ nm, for spheres 11–20 $a=50$ nm, for spheres 21–30 $a=20$ nm, for spheres 31–40 $a=50$ nm, and for spheres 41–50 $a=100$ nm. The x coordinate of the first sphere is $x_1=5000$ nm. The distance between the tenth and 11th spheres (the same as those between the 20th and the 21st, the 30th and the 31st, the 40th and the 41st) is 1000 nm.

We organize the paper as follows. In Sec. II, we describe our model, and establish the equation set for the local field at dipole sites. We outline expressions for the surface-plasmon field and explain how to apply the field expressions to obtain the self-consistent local field. Various resonances in the system are pointed out and discussed. In Sec. III, we introduce a formalism to describe the field propagation stemming from a dipole in which propagating homogeneous waves and evanescent field are separated. Sec. IV is devoted to numerical studies of field distribution for up to 100 dipoles near the surface. Assuming the dipoles are mesoscopic silver spheres placed on a silver surface, we present numerical results for different parameters of the model system. We discuss how and under what conditions the local field would be dramatically enhanced, and in what cases the radiation is primarily a propagating wave in the far-field zone, and in what cases the radiation is concentrated around the scattering centers (optical near-field localization). Finally, we present a numerical modeling of the NSOM for the scattered surface polariton measurements. The results are compared with existing experimental data.

II. LOCAL FIELD AT DIPOLE SITES UNDER SURFACE POLARITON EXCITATION

Our task in the present paper is to study the distribution of the scattered field in the vacuum half-space and immediately above the surface. In our model of SP scattering, the surface polariton is assumed to travel along the x axis from the minus infinite $-\infty$ to plus infinite $+\infty$ (Fig. 1). The surface

scatterers are represented by a few pointlike electric dipoles distributed above the substrate. For a perfect flat surface, the SP's cannot escape from the surface, and the field immediately adjacent to the surface is an evanescent field. This evanescent field is the external field driving the dipoles. The excited dipoles are strongly influenced by their surroundings. The optical coupling between the dipoles and the coupling via the substrate (together with the screening effects if the dipoles are more realistically replaced by finite-size particles) establish a local field at the dipole sites. This modified local field causes the dipole to radiate. A summation of all dipole radiation at observation point $\vec{r}$ in our Cartesian coordinate in Fig. 1 yields the whole scattered field $\vec{E}(\vec{r})$. For N dipoles the summation is[32,33]

$$\vec{E}(\vec{r})=\vec{E}_0(\vec{r})-\mu_0\omega^2\sum_{i=1}^{i=N}\overleftrightarrow{G}(\vec{r},\vec{r}_i)\cdot[\overleftrightarrow{\alpha}_i\cdot\vec{E}_{\rm local}(\vec{r}_i)], \quad (1)$$

where μ_0 is the permeability of vacuum, and ω is the light angular frequency. $\vec{E}_0(\vec{r})$ is the field which would prevail in space if the scattering sources were absent, $\overleftrightarrow{G}(\vec{r},\vec{r}_i)$ is a Green's function (namely, the field propagator[39]) which describes the field propagation from the ith dipole at point $\vec{r}_i$ to the observation point $\vec{r}$. Finally, $\overleftrightarrow{\alpha}_i$ is the polarizability of the ith dipole which bears a local field as $\vec{E}_{\rm local}(\vec{r}_i)$. This local field has to be calculated in a self-consistent way, and together with the polarizability determines the final current density at the dipole in question.

A. Self-consistent field equations

In the system shown in Fig. 1, the only scattering centers are the dipoles. To determine the local field at each dipole, for N dipoles one writes down a set of self-consistent equations,[32,33] i.e.,

$$\vec{E}_{\rm local}(\vec{r}_i)=\vec{E}_0(\vec{r}_i)-\mu_0\omega^2\sum_{j=1}^{j=N}\overleftrightarrow{G}(\vec{r}_i,\vec{r}_j)\cdot[\overleftrightarrow{\alpha}_j\cdot\vec{E}_{\rm local}(\vec{r}_j)]$$

$$i=1,2,\ldots,N; \quad (2)$$

or omitting the label *local* and introducing a supermatrix $\mathcal{F}$ and supervectors $\mathcal{E}_0$ and $\mathcal{E}$, respectively, Eq. (2) can be written in more convenient way as

$$\mathcal{E}=\mathcal{E}_0+\mathcal{F}\cdot\mathcal{E}. \quad (3)$$

Our way to solve the above equation is rigorous and straightforward,[32,33] i.e.,

$$\mathcal{E}=[\mathcal{U}-\mathcal{F}]^{-1}\cdot\mathcal{E}_0, \quad (4)$$

where $\mathcal{U}$ is a unit matrix.

B. Surface-plasmon polariton

As for the background field $\mathcal{E}_0$ in Eq.(4), we consider the field of the surface polariton. The typical surface wave for a smooth surface can be expressed as[2]

$$\vec{E}(x,z)=\vec{E}_0^{\pm}e^{ik_x x\pm|k_z|z}, \quad (5)$$

with $+$ for $z\geqslant 0$ in the vacuum, and $-$ for $z\leqslant 0$ in the metal. k_x in Eq. (5) is the polariton wave vector, which can be obtained from the dispersion relation, i.e.,

$$k_x^2=\left(\frac{\omega}{c_0}\right)^2\frac{\epsilon}{1+\epsilon}, \quad (6)$$

where c_0 is the light speed in vacuum, and ϵ is the dielectric function of metal. The decaying factor k_z can also be obtained by

$$k_z^2=k_x^2-\left(\frac{\omega}{c_0}\right)^2\begin{cases}1 & \text{in vacuum}\\ \epsilon & \text{in metal.}\end{cases} \quad (7)$$

The field $\vec{E}_0$ in the vacuum (in our calculation, we will need only the field in the vacuum) lies in the x-z plane. The proportion of the z and x components can be obtained from the relation $\mathrm{div}\vec{E}=0$, i.e.,

$$E_z=i\frac{k_x}{k_z}E_x. \quad (8)$$

Usually, the relation $E_z\gg E_x$ is satisfied, but only for very long wavelengths do the two components become comparable.

The overall picture of the surface polariton is that the maximum SP field is on the surface, and decays exponentially along $+z$ in the vacuum with a relatively longer tail, and along $-z$ in the metal with a shorter penetrating depth into the metal. The propagation along the x axis damps out within a so-called propagating length L which can be related to the imaginary part of k_x, as $L=[2\mathrm{Im}\{k_x\}]^{-1}$. Except for very long light wavelength, the field is primarily in the z direction.

C. Field enhancement in the dipole-surface system

In this subsection we discuss the possible enhancement of the local field at the dipole sites. The enhancement refers to the changes of the field at the dipole sites calculated self-consistently according to the equation set in Eq. (2) with all the optical coupling between the objects in the system taken into account.

For the individual scatterer, in a realistic case when the dipole is replaced by a mesoscopic particle, there are mainly two kinds of resonance, namely, the plasmon resonance of the particle stemming from the internal collective electron coupling (intraband transition),[40] and the resonance due to couplings between discrete energy states for quantum particles (interband transition).[41] In a previous paper,[33] we discussed in detail the frequency and size dependence of the particle plasmon in a sphere-surface configuration. In the present work, we shall fix the light frequency ($\lambda=632.8$ nm). As interband transitions usually occur at much higher frequency for particles with sizes of interest, we shall not consider the modes in the spheres, and shall use for a spheric particle of radius a the following well-known expression for the polarizability:

$$\overleftrightarrow{\alpha}(\omega)\equiv\alpha_0(\omega)\overleftrightarrow{U}=4\pi\epsilon_0 a^3\frac{\epsilon(\omega)-1}{\epsilon(\omega)+2}\overleftrightarrow{U}, \quad (9)$$

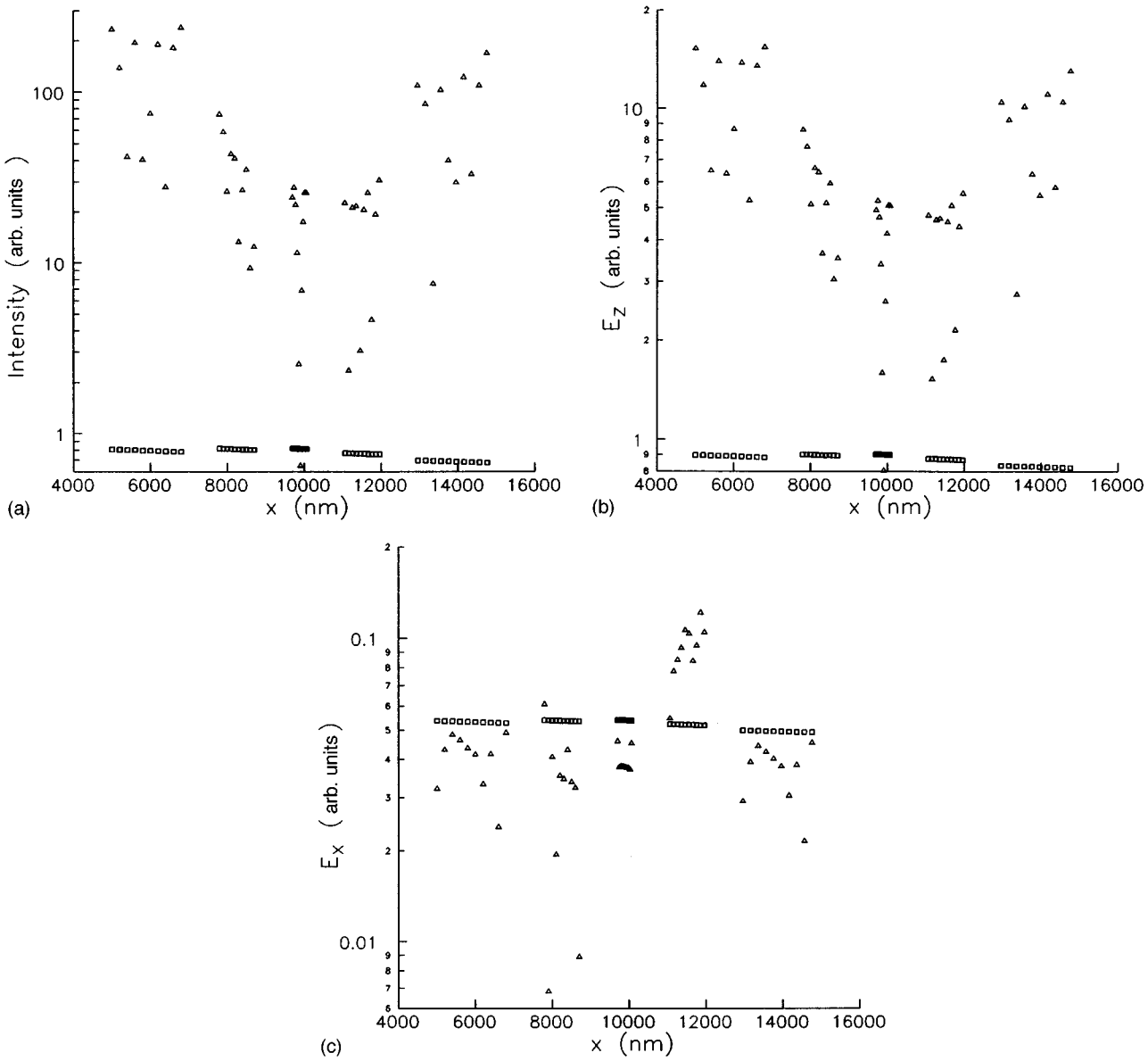

FIG. 2. Local-field distribution at the sites of the 50 spheres in Fig. 1 under the excitation by the surface polariton traveling from $-\infty$ to $+\infty$. The intensity of the SP field at the origin point is assumed $I_0=1$. (a) Total field intensity, (b) E_x, and (c) E_z field components, respectively. □ represents the initial field $\vec{E}_0$, and △ is the calculated local field $\vec{E}_{\text{local}}$. The y scale is logarithmic.

where $\overleftrightarrow{U}$ is a unit tensor, and the dielectric function $\epsilon(\omega)$ is to be chosen from experimental data for the frequency used for numerical calculations.

The resonance condition of the whole N-dipole–surface system hides in Eq. (4) symbolically, i.e.,

$$\mathcal{U}-\mathcal{F}=0\,, \tag{10}$$

which includes the direct coupling between dipoles and the indirect coupling via the surface. We previously referred to the resonances derived from Eq. (10) as configurational resonances (see Ref. 33 and 32). In numerical studies, for more than two dipoles it is difficult to approach the resonances, because one cannot solve the resonant condition analytically; however, for one or two dipoles, it is possible to calculate the length of resonance coupling exactly. In the following we shall point out the two most important kinds of coupling.

One of the most important couplings is the coupling of the dipole via the surface reflection to the dipole itself. This coupling is known as surface dressing effect. In Eq. (10), for a system of only one dipole, one obtains the local field at the dipole, and realizes that at certain distances the local field can be resonantly enhanced. Note that the field propagator $\overleftrightarrow{G}_{ii}$ in Eq. (10) describes this surface dressing effect. Before considering couplings with other dipoles in the system, one calculates the surface dressing first, and incorporates this modification into the dipole polarizability. When calculating the dipole radiation, the surface reflection is replaced equivalently by the radiation of an image mirror dipole in the metal. Detailed processes to calculate the modified polarizability and related discussions may be found in Refs. 33 and 32. In a sphere-surface system, important modifications happen when the dipole-surface separation δ reaches some resonance distances, i.e.,[33]

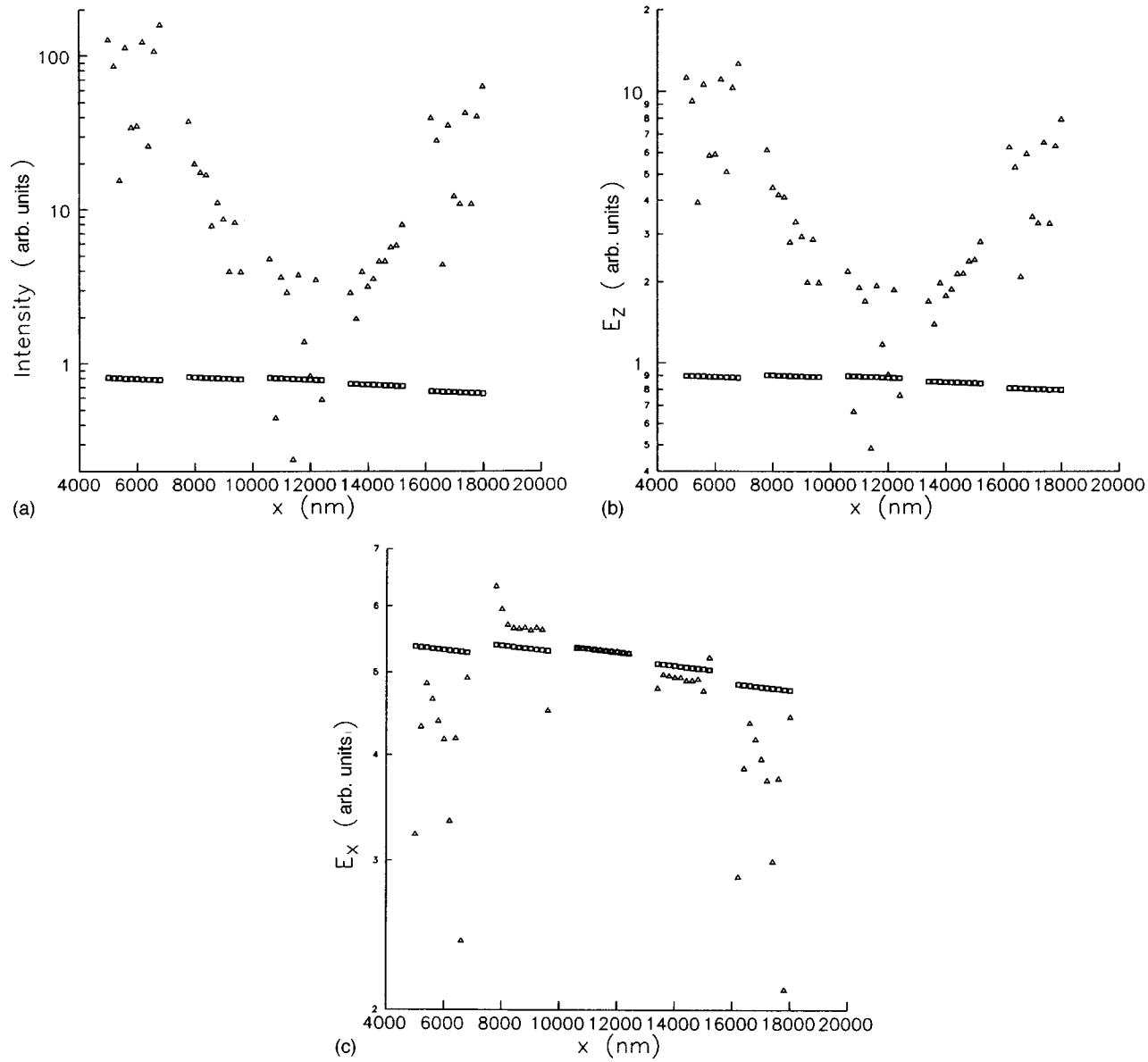

FIG. 3. Local-field distribution at the sites of the 50 spheres in Fig. 1, but the center-center distance $L=200$ nm for all the spheres. Notations are the same as those in Fig. 2.

$$\delta_r=[|A|^2/(16\pi\epsilon_0\mathrm{Re}\{A\})]^{1/3}, \tag{11}$$

where $A\equiv\alpha_0(\omega)r^p(\omega)$, and $r^p(\omega)$ is the p-polarized reflection coefficient for the surface and can be calculated from the bulk dielectric function $\epsilon(\omega)$ as $r^p(\omega)=[\epsilon(\omega)-1]/[\epsilon(\omega)+1]$. In the above equation, assumed a short distance between the dipole and the surface ($\delta\ll\lambda$), or considered only the $1/r^3$ term in the nonretarted ($c_0\to 0$) field propagator. The resonance condition in Eq. (11) is associated with the field component in the z direction (perpendicular to the surface). Other resonance distances associated with the field components in parallel (to the surface) directions can be similarly estimated,[33] and they are much shorter than the resonance distance in Eq. (11).

The second important coupling is the coupling between the two neighboring dipoles. We shall omit indirect coupling (via the surface reflection) between the two dipoles. This omission could be justified by our previous numerical calculations.[32] Similar to the above dipole-surface coupling, when the dipole-dipole distance L is at short range (less than a wavelength), the coupling becomes mainly evanescent and the resonance coupling occurs at the distance determined by

$$L_r=(|A|^2/[(2\pi\epsilon_0)^2\mathrm{Re}\{A\}])^{1/6}, \tag{12}$$

where $A\equiv\alpha_1(\omega)\alpha_2(\omega)$, $\alpha_1(\omega)$ and $\alpha_2(\omega)$ are the polarizability of the two dipoles, respectively, and $\mathrm{Re}\{A\}>0$ is required to match the resonance.[42]

In the numerical calculations (Sec. IV), we used various distances (δ and L), and the radius of the spheres, a. The latter changes the polarizability and, thus, the value of A in the above formulas. Due to the fact that resonance conditions in the whole system are dependent on many parameters, it is difficult to study all the contributions. However, the resonant distances estimated with the above formula concerning only one or two dipoles should still be good references to the

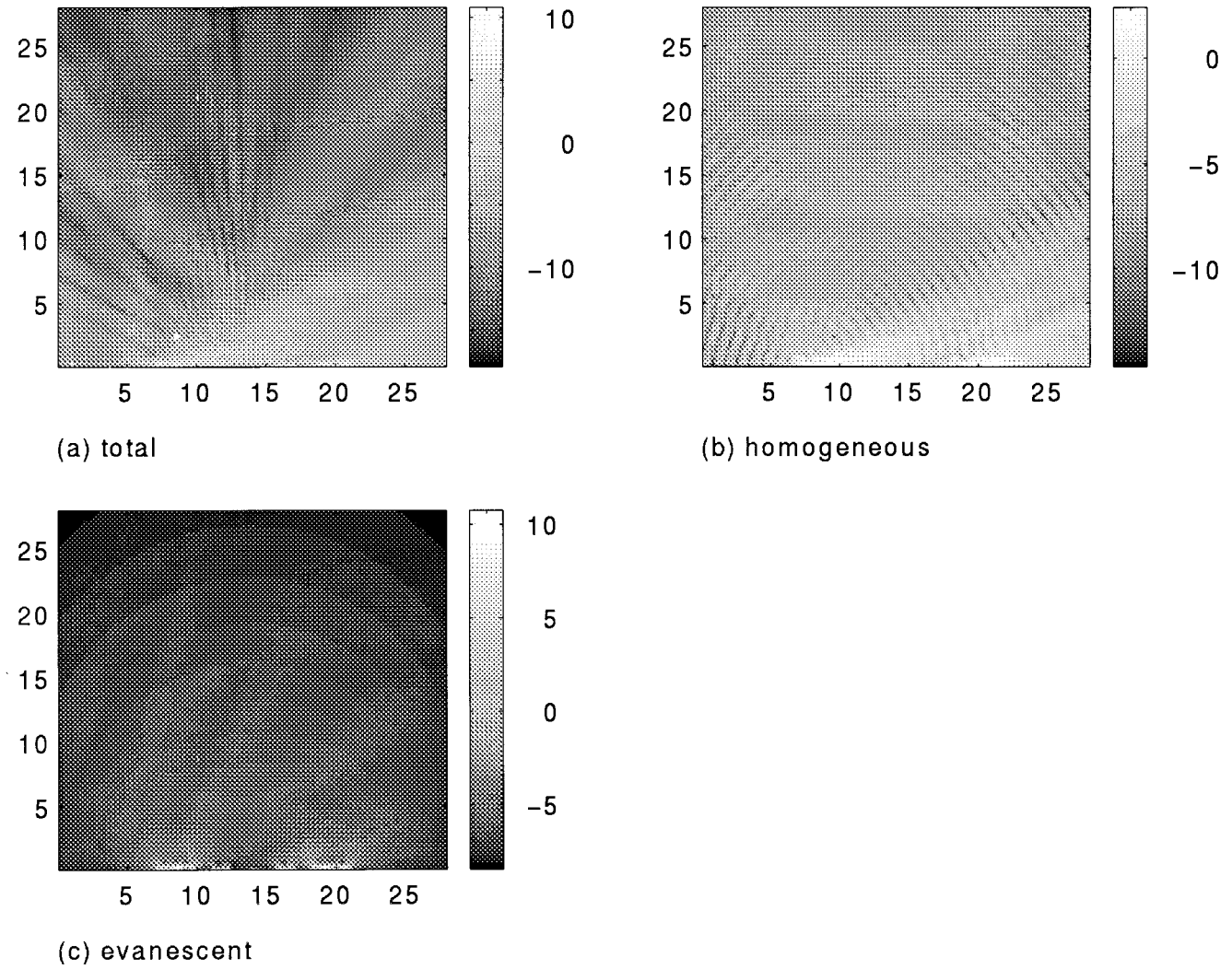

FIG. 4. x-z intensity distribution for the system in Fig. 1. The x-y scale is normalized to the wavelength λ. The gray scale is logarithmic.

enhancement of the local field in the whole system when all objects are included in the calculation, and the full field propagators are adapted without taking the approximations, which lead to the simple relations in Eqs. (11) and (12). In Sec. IV, we shall point out that, in general, the local-field enhancement occurs at the dipoles for which the resonance conditions in Eqs. (11) and (12) are approximately approached.

III. HOMOGENEOUS AND INHOMOGENEOUS FIELD RADIATION

In Sec. II, we showed how to calculate the local field at the dipole sites. We also gave the necessary expressions for the polarizability and the background field of the surface polariton. Finally, to calculate the radiation in the vacuum half-surface with basic equations Eq. (1), we have to know the propagation behalf $\overleftrightarrow{G}(\vec{r},\vec{r}_i)$.

In the following, we outline the formalism for the field propagator and its decomposed homogeneous and inhomogeneous parts. The homogeneous part, which contains only the propagating waves, is the part one wants to avoid in near-field optics. The inhomogeneous part, which contains only the so-called evanescent field, is the useful part for retrieving the subwavelength details in NSOM. It can be demonstrated[36] that the diffraction of a homogeneous field gives exactly the classic Rayleigh limit, while an inhomogeneous field is not subject to this limit. In the case of a single dipole (and if the dipole is placed at the origin point), the field propagator has the well-known dyadic form[32,33,39]

$$\overleftrightarrow{G}(\vec{r})=\frac{1}{4\pi}\left[\left(-\frac{1}{r}-\frac{ic_0}{\omega r^2}+\frac{c_0^2}{\omega^2 r^3}\right)\overleftrightarrow{U}+\left(\frac{1}{r}+\frac{3ic_0}{\omega r^2}-\frac{3c_0^2}{\omega^2 r^3}\right)\vec{n}\vec{n}\right]e^{i(\omega/c_0)r}, \tag{13}$$

where $\vec{n}$ is a unit vector in the $\vec{r}$ direction.

We recently realized the exact decomposition of the above field propagator into its homogeneous and inhomogeneous parts. The decomposed propagators were employed to discuss various aspects in near-field optics, such as the resolution limit[36] and resonances.[37] The decomposition process can be briefly described as follows.

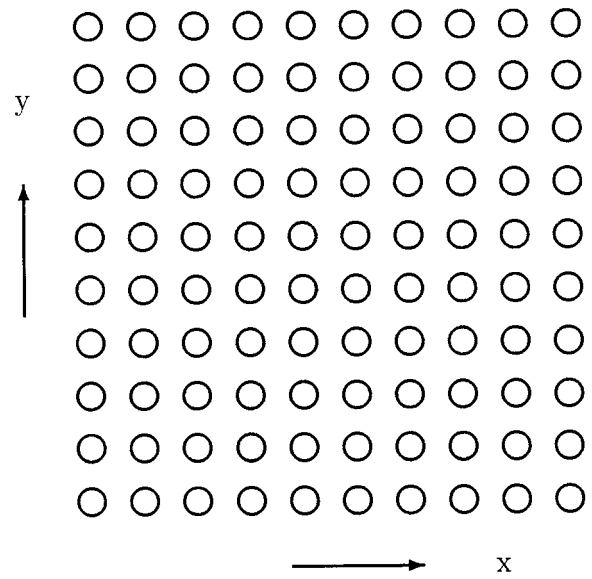

FIG. 5. Scheme of the system of 10×10 spheres with the radius $a=100$ nm, center-center distance $L=200$ nm, and center-surface separation $\delta=100$ nm. The first sphere (left-down) is placed at $x,y=500$ nm.

In a plane-wave expansion along the x-y plane, the field propagator for a wave number along the plane, $q_\parallel$, can be written as[39]

$$\overleftrightarrow{G}(z,\vec{q}_\parallel,\omega)=\frac{e^{iq_z z}}{2iq_z}[\vec{e}_y\vec{e}_y+\vec{e}\vec{e}], \tag{14}$$

where vectors $\vec{e}_y=(0,1,0)$, $\vec{e}=(c_0/\omega)(-q_z,0,-q_\parallel)$, and $q_z^2=(\omega/c_0)^2-q_\parallel^2$ The field at an observation point in space at $\vec{r}$ is a summation of the plane waves described in Eq. (14) for various wave numbers $q_\parallel$. However, it is easy to see that for $0<q_\parallel\leqslant\omega/c_0$ the plane waves are homogeneous (propagating), and thus can go far away from the dipole (far field zone), and for $\omega/c_0<q_\parallel<\infty$ the plane waves become inhomogeneous (evanescent) and stay within a short distance from the dipole (near field zone) (see Ref. 43 for a general discussion). That is, in the near field the evanescent field dominates, whereas in the far field the homogeneous waves dominate. An extensive discussion and background information concerning the theory of the decomposition are to be published in Ref. 38.

The field propagator in real coordinate $\overleftrightarrow{G}(\vec{r},\omega)$ is a summation (inverse Fourier transform) of the plane waves in Eq. (14), i.e.,

$$\overleftrightarrow{G}(\vec{r},\omega)=\frac{1}{(2\pi)^2}\int_{(R)}\overleftrightarrow{S}^{-1}\cdot\overleftrightarrow{G}(z,\vec{q}_\parallel,\omega)\cdot\overleftrightarrow{S}e^{i\vec{q}_\parallel\cdot(x\vec{e}_x+y\vec{e}_y)}d^2q_\parallel, \tag{15}$$

where $\overleftrightarrow{S}$ is a tensor, for the sake of convenience, to rotate the coordinate system [from $(q_x,q_y,0)$ to $(q_\parallel,0,0)$], which has a form

$$\overleftrightarrow{S}=\frac{1}{q_\parallel}\begin{bmatrix} q_x & q_y & 0\\ -q_y & q_x & 0\\ 0 & 0 & q_\parallel\end{bmatrix}, \tag{16}$$

and the integration range (R) is chosen $0-(\omega/c_0)$ for homogeneous $\overleftrightarrow{G}_h$, $(\omega/c_0)-\infty$ for inhomogeneous $\overleftrightarrow{G}_i$, and $0-\infty$ for the total field propagator $\overleftrightarrow{G}$.

For the total field the integration retrieves the expression in Eq. (13). The resulting inhomogeneous propagator can be written as

$$\overleftrightarrow{G}_i(\vec{r},\omega)=\frac{1}{4\pi}\left[\left(-\frac{1}{2r}+\frac{c_0^2}{\omega^2r^3}\right)\overleftrightarrow{U}+\left(-\frac{1}{2r}-\frac{3c_0^2}{\omega^2r^3}\right)\vec{n}\vec{n}\right]. \tag{17}$$

The homogeneous propagator can be obtained either by a direct integration over the range $0\sim(\omega/c_0)$ or by $\overleftrightarrow{G}_h=\overleftrightarrow{G}-\overleftrightarrow{G}_i$. The above results have been discussed in detail elsewhere.[36–38] Here we employ the formulas for studying the SP scattering.

IV. NUMERICAL STUDIES AND DISCUSSION

In this section, we present numerical results obtained by using equations introduced in preceding sections. As already mentioned, in numerical calculations we replaced the dipoles with spheric silver particles, of which the polarizability can be calculated with the expression in Eq. (9). The surface is also assumed to be of silver. The frequency of the incident light is chosen $\lambda=632.8$ nm, and the corespondent dielectric function for silver is chosen from the experimental data in Ref. 44 (refractive indexes of silver $n=0.06+i4.15$). The numerical calculations were carried out systematically for various parameters and geometries of the dipole system. Gray-scale pictures made in Matlab are used to present the field intensity distributions.

A. Local field at dipole sites

The first system we have studied is shown schematically in Fig. 1, which consists of 50 silver spheres placed on top of a silver surface. The background field is the surface polariton travelling from $-\infty$ to $+\infty$. In order to have a reference value for the field, we assumed a unit electric field at the origin point $|\vec{E}_0(x=0)|=1$. Without the spheres this field decreases exponentially in the $+x$ direction. The presence of the scatterers changes the local-field distribution dramatically. The modification can be calculated with the self-consistent field equations introduced in Sec. II.

In Fig. 2 we plot the calculated local field in comparison with the background field, which is calculated by using Eq. (5) for the SP field. The intensities of the background and local fields are presented in Fig. 2(a). (Note that the steps in the background field from one sphere chain to another are due to the changes of the sphere z coordinate.) At some spheres, particularly the spheres with radius of 100 nm, the field is enhanced dramatically, while at other spheres the enhancement is relatively weaker, and even negative for some smaller spheres. The main reason of the enhancement is that the optical coupling of the larger spheres ($a=100$ nm) with their immediately neighboring spheres is much stronger

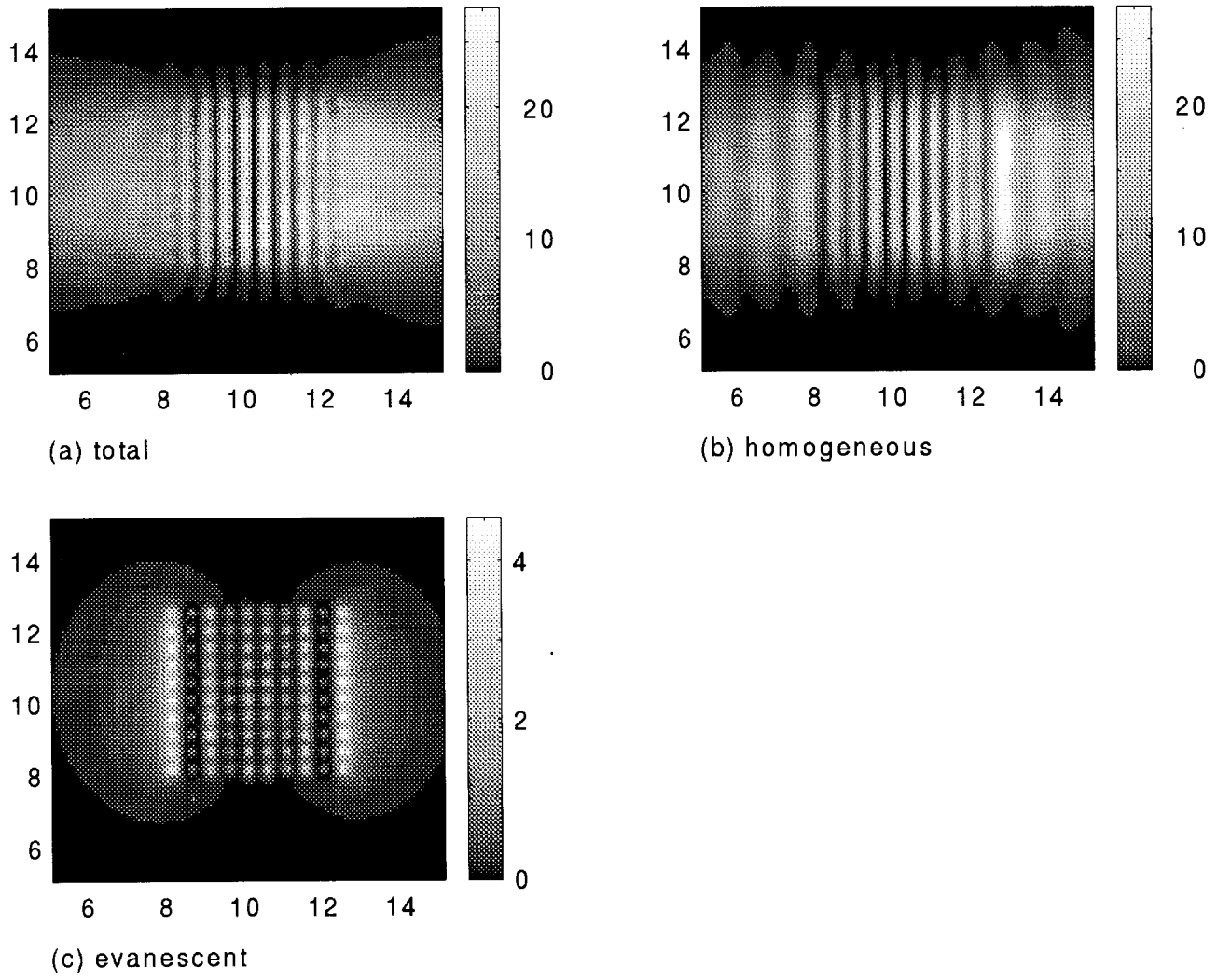

FIG. 6. x-y intensity distribution at $z=300$ nm distance from the surface for the system in Fig. 5. The scale is normalized to λ. The SP propagates from left to right.

than that of the smaller spheres. Both the polarizability and distances [δ and L in Eqs. (11) and (12)] should have played important roles.

It is interesting to see the modification separately in the field components in parallel (E_x) and perpendicular (E_z) directions. In Figs. 2(b) and 2(c), the magnitude of the field components $|E_x|$ and $|E_z|$ are presented respectively. The significant variation of the field across the chain of the spheres is observed in all cases, but the variations of the E_z component is stronger than the E_x component in all the cases. Moreover, for the chain of smallest spheres the changes of E_z along the chain is almost two orders of magnitude stronger than for the chains consisting of larger spheres. The absolute value of the enhancement of the field component in the perpendicular direction E_z is much stronger than that in the parallel direction. As already mentioned in Sec. II, the resonance distance δ_r associated with the field component E_z in Eq. (11) (see also Ref. 33 for a detailed discussion) is longer than those associated with other field components. With a fixed light frequency and the use of a simple expression for the polarizability, none of the resonances (for the individual dipole-surface coupling) can be

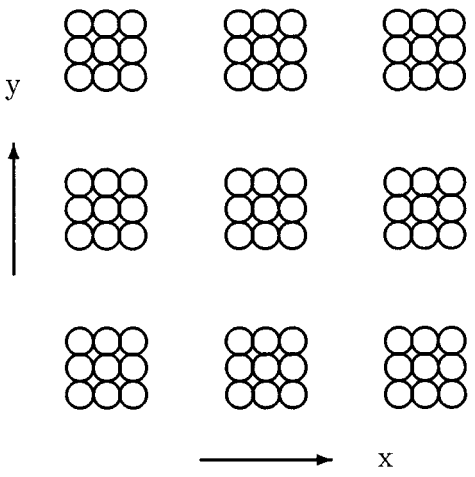

FIG. 7. Scheme of the system of 9×9 spheres with the radii $a=20$ nm, center-center distance $L=40$ nm, center-surface separation $\delta=20$ nm, and edge-edge distances between the 3×3 unit are 150 nm. The first sphere (left-down) is placed at $x,y=50$ nm.

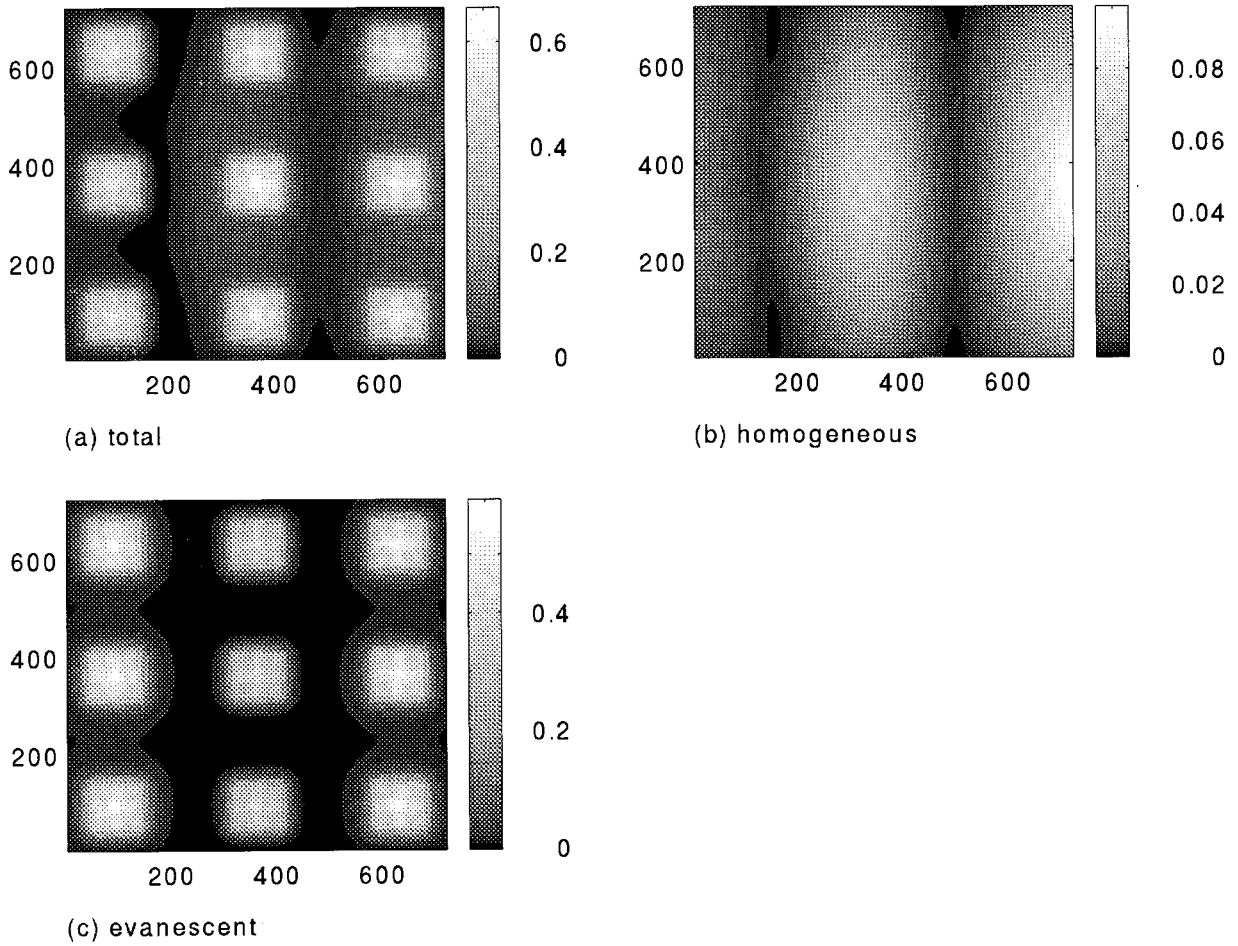

FIG. 8. x-y intensity distribution at $z=60$ nm distance from the surface for the system in Fig. 7.

exactly matched. However, with a longer resonance distance, the resonance condition for the field component E_z is approached more closely than those for other components. This explains the differences in Figs. 2(b) and 2(c). In the SP field the dominating field component is in perpendicular direction, and more likely the SP field is enhanced by surface particles with strong particle-surface coupling. A strong E_z results in a strong evanescent field near the scatterers and, therefore, strong scattering into surface polaritons (while E_x would bring out propagating waves in the far field zone) as was pointed out in Sec. III.

In order to study the influence of the coupling between the spheres, in Fig. 3 we plot the local-field distribution for the same system as that in Fig. 1, but the sphere-sphere distance is adjusted to be equally $L=200$ nm. Apparently from the figures in Fig. 3, the field enhancement is reduced in comparison with that in Fig. 2, which should be attributed to the relatively longer sphere-sphere distances, or it is demonstrated the importance of the coupling between the spheres. An interesting remark can be drawn from both Fig. 2 and Fig. 3: the field enhancement is more likely to happen at the edges of the dipole chain, while in the middle of the chain the field is reduced. Similar phenomena can also be observed in the figures presented in the forthcoming subsections.

In summary, the surface scatterers dramatically change the local-field distribution for both E_x (parallel to the surface) and E_z (perpendicular to the surface) field components, and these changes are different for different field components. For a SP field, the field component in the perpendicular direction is dramatically enhanced due to the strong coupling between the spheres and the surface and between the neighboring spheres. The observed strong variation of the field across the chain of spheres particularly offers an explanation for the experimentally observed phenomenon that the NSOM images of the SP field distribution over a rough surface do not coincide with the surface profiles.[22,23,25]

The local field at the sphere sites causes the dipoles to radiate. In Sec. IV B we shall demonstrate the far-field leakage as well as the strong evanescent field presence in the near-field area due to the radiation.

B. x-z intensity distribution

In this subsection, we present the field intensity distribution in the x-z plane (perpendicular to the surface) for the system in Fig. 1. We present separate distributions for the propagating waves, evanescent field, and total field. The distributions were calculated with the decomposed field propagators introduced in Sec. III.

In the calculated figures (Fig. 4) one can clearly see the change of the field intensity when the distance from surface increases. In the image obtained only with the propagating

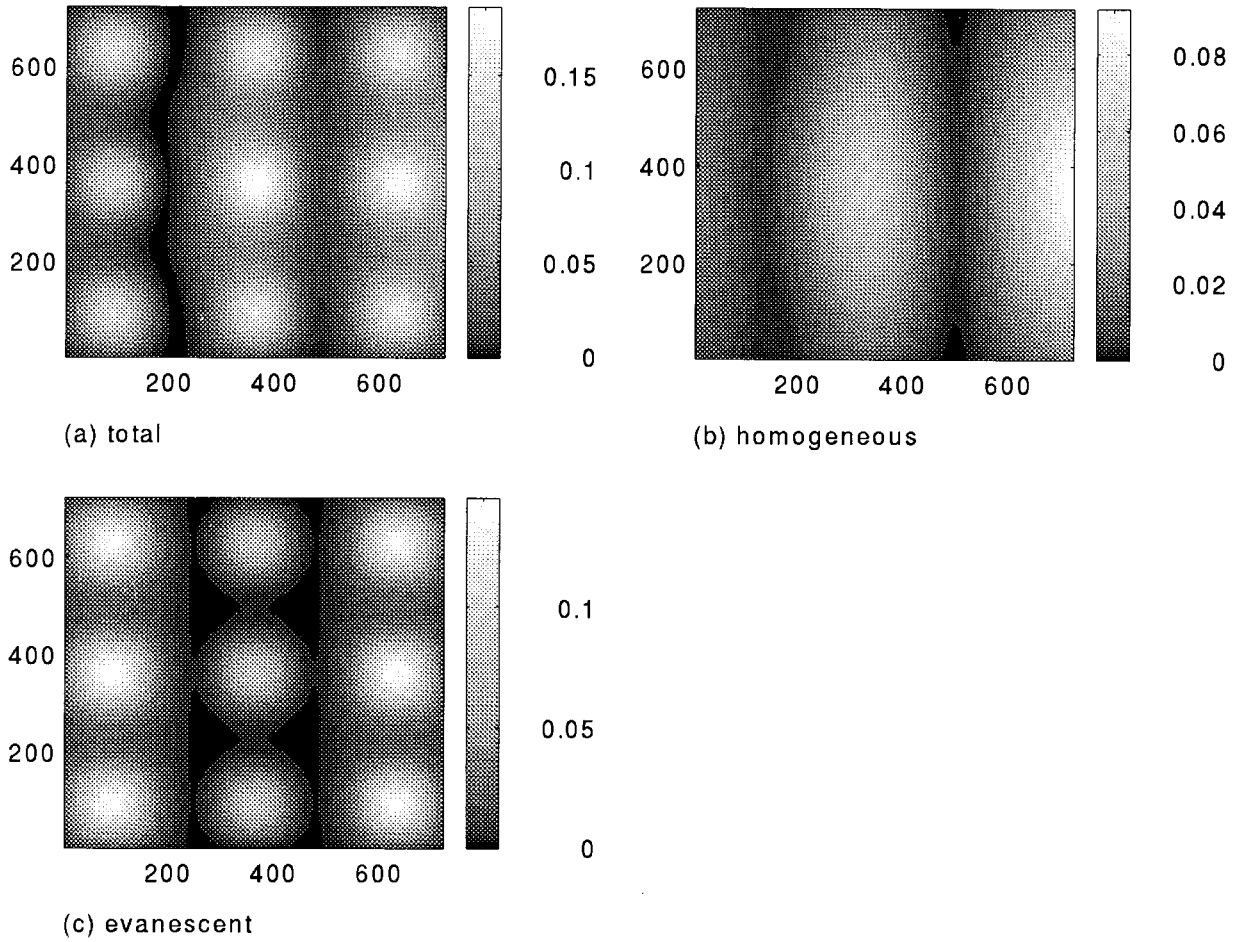

FIG. 9. x-y intensity distribution at $z=100$ nm distance from the surface for the system in Fig. 7.

waves, the separations between the spheres can hardly be seen due to the diffraction of the propagating waves, so only the diffraction pattern is presented in the propagating wave distribution. In the evanescent field distribution the separate spheres could be resolved at short distances from the surface, while at some (still short) distances prominent dark-bright spots can be observed along the sphere chains corresponding to the strong local-field variation even along the chain of the same spheres, which, as already pointed out, confirms that the SP field distributions over rough surfaces are not correlated with the surface topography.

Several bright-dark slits are also observed in the total field distribution, which we have attributed to the interferences between the evanescent field and the propagating waves[36] because of the fact that the total intensity is not only the simple summation of the evanescent and propagating intensities. The position of the slits depends significantly on the distance from the surface as the phase factor changes with the distance.

In summary, for a chain of mesoscopic scatterers with subwavelength separations, a strong evanescent field would be established near the scatterers while strong propagating waves would escape from the surface mainly at the edges of the chain. The field around the scatterers changes due to the uneven distribution of the local field at the sphere sites. The interferences between the evanescent field and the propagating waves may bring about interference patterns even in the far-field zone, which is not necessarily consistent with the surface profile, but it would bring out some information about the subwavelength features in the surface.

C. x-y intensity distribution

As far as the optical near-field localization and NSOM are concerned, one is interested in calculating the lateral field distribution over the surface (in the x-y plane), especially for surface-observation plane distances shorter than the light wavelength. For this purpose, we carried out calculations for two different arrangements of the surface scatterers. In the following figures the direction of the surface polariton propagation is from left to right.

In Fig. 5, we consider 10×10 spheres of radius $a=100$ nm distributed rectangularly in the x-y plane along the surface with equal center-surface distance $\delta=100$ nm and center-center separations $L=300$ nm. The observation plane is placed 250 nm above the substrate. The resulting images are shown in Fig. 6 for distributions of the propagating waves, evanescent field, and total field. The resolution seems to be much better in the direction of the SP propagation (x direction) than the y direction (perpendicular to the SP propagation). In the y direction there is a strong presence of the propagating waves which causes the smearing out of the

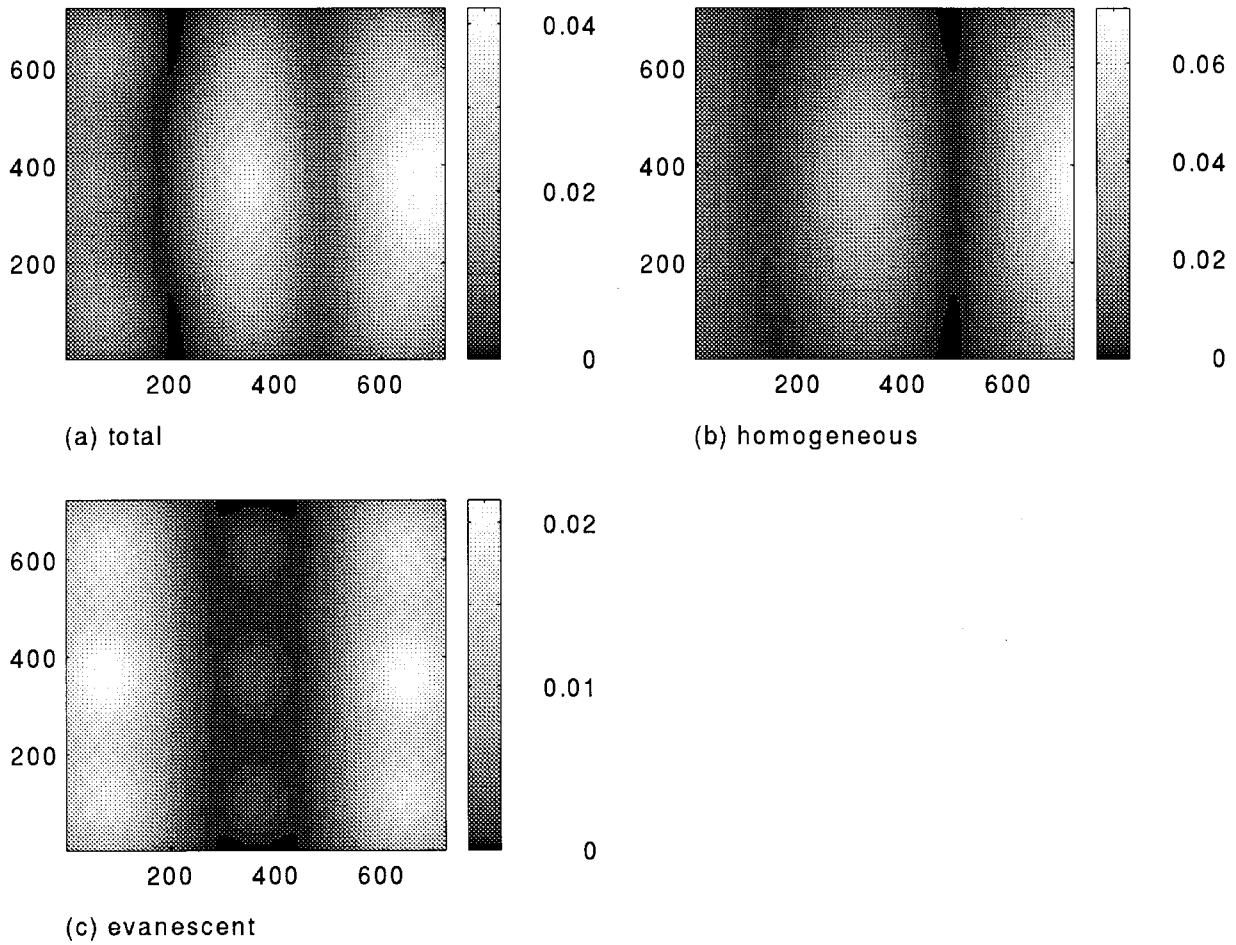

FIG. 10. x-y intensity distribution at $z=200$ nm distance from the surface for the system in Fig. 7.

separations between the spheres. The strong propagating waves escaping in the two sides of the rectangular system in the x direction raise difficulties in resolving the surface details in the total field distribution. Only the evanescent field distribution shows a fair agreement with the surface features, though even in this distribution [Fig. 6(c)] the image is distorted with respect to the topography. The strong scattering of the SP's results in far-field leakage in the two sides of the system in the x direction. The resolution is much better in the x direction than in the y direction even for the propagating waves. The evanescent field is dramatically changed due to the optical coupling in the system. Thus even the evanescent field distribution cannot offer a consistent topographic image, though the resolution in the evanescent field distribution is much better than that in the propagating wave distribution.

Let us consider an arrangement with smaller features. In Fig. 7, nine units of 3×3 spheres of parameters $a=20$ nm, $L=40$ nm, and $\delta=20$ nm are distributed with unit-unit distance 150 nm (sphere edge to edge). Intensity distributions were calculated for the observation plane being at three z distances, 60, 100, and 200 nm, and the results are presented in Figs. 8, 9, and 10, respectively.

For shorter observation distances the small units (roughly correspondent to a 120×120 nm^2 object) are completely resolved (Figs. 8 and 9), while for the largest distance of 200 nm (which corresponds roughly to $\lambda/3$) these units are not resolved even in the evanescent image (Fig. 10). The spheres that compose the units are only resolved in Fig. 8 for the smallest observation distance. Thus the resolution should be attributed to the strong presence of the evanescent field at short distances from the scatterers. The resolution decreases when the homogeneous field becomes dominant.

It is a very interesting question whether it is possible to selectively detect the evanescent field. Moving the local probe close to the sample and making the probe tip extremely small are two possible ways to achieve this purpose. How to pick up the evanescent field from the total field remains an unsolved problem, however. The study of this issue is outside of the scope of the present paper. Some relevant discussions may be found in Ref. 37.

It is worthy pointing out that in Figs. 9 and 10 the evanescent field at the center three units (second column) are relatively much weaker than the field at other units. Relevantly we mention that the inconsistency of the surface objects with the radiated near field is one of the important experimental findings.[22,23]

D. Numerical model of NSOM

In this subsection, we numerically model the NSOM device. We introduce a scanning local probe tip into the dipole system. Our purpose is to see the influence of the local probe on the field distribution.

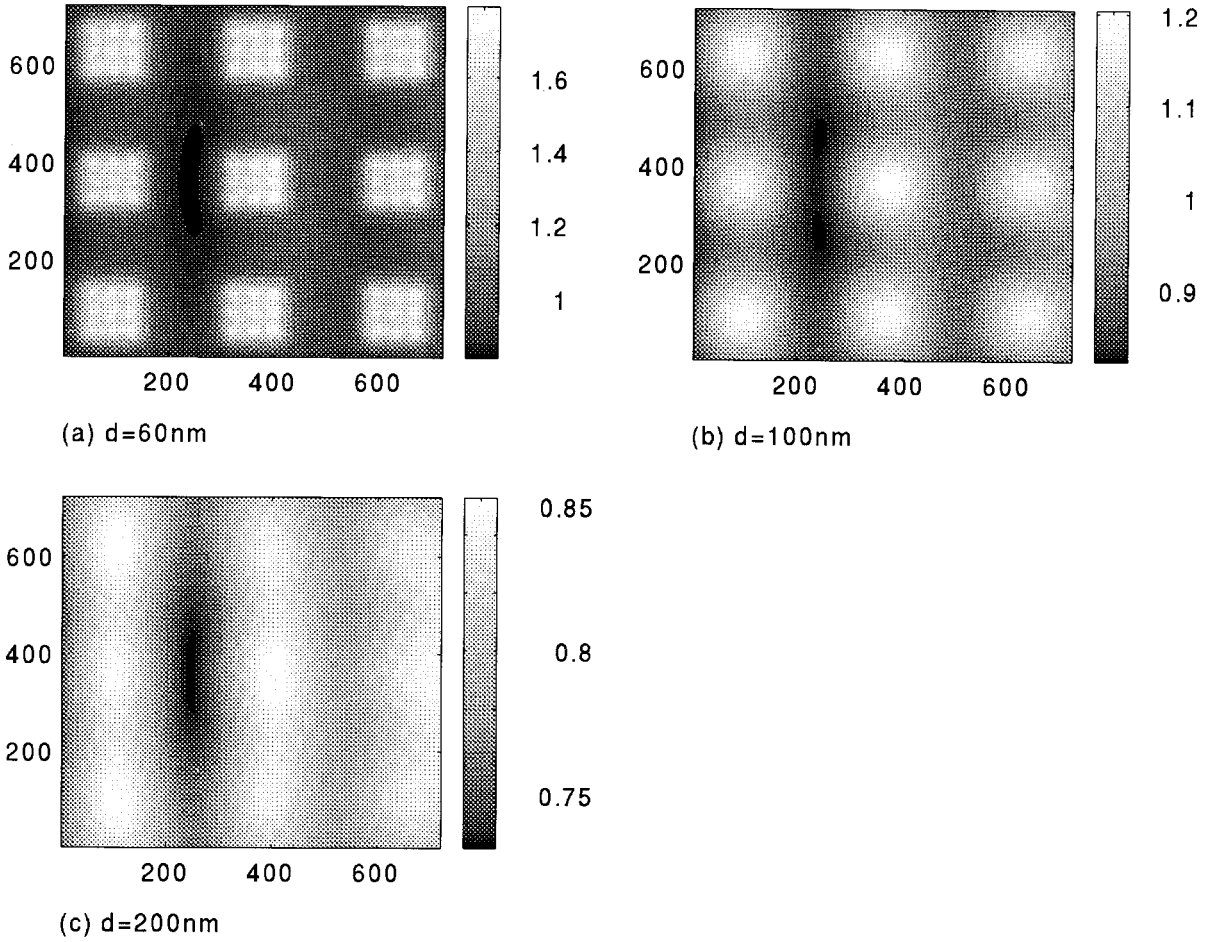

FIG. 11. Local-field intensity at the probe tip (glass sphere of $a=20$ nm) scanning over the system in Fig. 7 at different distances from the surface: (a) $z=60$ nm, (b) $z=100$ nm, and (c) $z=200$ nm.

For small distances between the probe tip and the surface in the NSOM, the optical coupling between the probe and the surface (and/or between the tip and scatterers) plays an important role. Therefore, the system ''surface plus scatterers plus probe tip'' should be considered for the modeling of the NSOM, analogously to the system ''surface plus probe tip'' that is usually considered in modeling the scanning tunneling electron microscope, where electronic coupling between surface and tip is needed to be taken into account for adequate description. We introduce the probe tip into the self-consistent equation set in Eq. (2), and assume that the calculated local field at the probe tip is proportional to the received signals by the device.[33]

We previously pointed out that, for strong optical coupling between the probe and surface, the self-consistent field has to be calculated with the probe tip included.[33,32] We also justified both theoretically and experimentally[45] that at least for reflection mode near-field scanning optical microscopy, where an uncoated homogeneous probe tip is employed, it is appropriate to model the probe tip as a small sphere. In our calculations, we assumed the probe tip to be a glass (refractive index $n=1.59$) sphere of $a=20$ nm, which is a close situation to the experimental device.[22] The probe is scanned at a constant distance over the scatterer arrangement as in Fig. 7. The obtained optical images are presented in Fig. 11, for the tip-surface distances $z=60$, 100, and 200 nm.

A comparison between the images in Figs. 8(a), 9(a), 10(a) and 11 clearly demonstrates the influence of the local probe. With the probe tip taken into account, the resolution becomes better. The probe receives more light from the closest surface particles, which suggests that the individuality of the scatterers would be more important.

E. Comparison with experiment

It is interesting to compare the numerical results with the existing experimental findings. In papers[22,23] by Bozhevolnyi and co-workers, rough gold films were studied with roughness parameters analogous to those for the model systems in Figs. 1 and 7, namely, bump (pit) heights of 5–100 nm and lateral sizes of 50–1000 nm. Optical images obtained at these surfaces with the NSOM under surface polariton excitation exhibit, at short (5 nm) distances from the surface, the round bright spots where the signal is 5–8 times higher than average level. Moreover, the positions of the spots do not correlate with the roughness topography (see Fig. 3 in Ref. 23 and Fig. 3 in Ref. 22). Thus the behavior of the localized light spots observed in the experiments can be described at least qualitatively by our numerical results in Figs. 2, 3 and 4. Moving the probe tip away from the surface during the experiments (Fig. 5 in Ref. 23 and Fig. 2 in Ref. 22) the optical signal decreases and the bright spots smear out, as

described by the model calculation in Figs. 4, 8, 9, and 10. However, in the middle field, some features of the distribution are still observed which could correspond to the dark (bright) slits in the middle field distribution presented in Fig. 4(a).

The observed dependence of the average signal on the tip-surface separation (decreased by about a half of the value when the distance changes from 5 to 1000 nm) (Refs. 22 and 23) changes much more slowly than the calculated images in Figs. 8, 9 and 10, without the probe tip being taken into account. The intensity drops by about 20 times for the distances from 60 to 200 nm. When the probe tip is included in the model, the calculated distance dependence in Fig. 11 is slower and closer to the experimental results. This confirms that the probe tip strongly interacts with the scattering field, and bears strong influences of both the propagating and evanescent components in the total field.

V. CONCLUSION

In this paper, we presented a numerical study of the optical near-field localization caused by surface-plasmon polariton scattering on a metallic surface with mesoscopic scatterers. We have found that, for a network composed of subwavelength scatterers with subwavelength separations, the optical coupling between the scatterers are mainly caused by the evanescent field, and the coupling results in a dramatic change of the local-field distribution on the scatterer sites, especially in the cases where the resonance status of the network is approached. Numerical results show that the enhancement of the local field would reach several orders of magnitude. We have demonstrated with separate intensity distributions for the total field, propagating waves, and evanescent field that over the surface scatterers there is a strong evanescent field distributed unevenly according to the scatterer distribution, and that strong propagating waves would be reradiated from the surface mainly at the edge of a scatterer chain. Numerical results for two-dimensional scanning at short distances from the surface show that, very close to the surface, the evanescent field dominates, which provides the possibility of obtaining subwavelength resolution, while the propagating waves tend to smear out the subwavelength features. Calculated optical images do not coincide with topographical structure of the scatterers, which is in agreement with the existing experimental results.

We have pointed out that as far as NSOM is concerned, the resolution is better along the direction in which the surface polariton propagates than in the perpendicular direction. Finally, we demonstrated with a numerical modeling of the NSOM device that the interaction between the probe tip and the sample surface has to be taken into account when the probe-surface distance is short, which results in significant changes of the field distribution.

ACKNOWLEDGMENTS

Work by M.X. and J.S. was supported by DGAPA (UNAM) under Grant No. IN108995 and CONACYT, 1887P-E9507. The work of A.Z. was supported by JNICT under Contract No. PRAXIS XXI/BCC/4318/94. We thank Professor T. Leskova of the Institute of Spectroscopy, Troitsk, Russia, for reading the manuscript.

*Mailing address: Institute of Physics–UNAM, P.O. Box 439036, San Ysidro, CA 92143. Electronic address: mufei@ifuname.ifisicaen.unam.mx

[1] *Surface Polaritons*, edited by V. M. Agranovich and D. L. Mills (North-Holland, Amsterdam, 1982).

[2] H. Raether, *Surface Plasmons on Smooth and Rough Surfaces and on Gratings* (Springer-Verlag, Berlin, 1988).

[3] F. Abelés and T. Lopez-Rios, in *Surface Polaritons* (Ref. 1), p. 239.

[4] C. S. West and K. A. O'Donnell, J. Opt. Soc. Am. A **12**, 390 (1995); R. E. Luna, E. R. Méndez, J. Lu, and Z. Gu, J. Mod. Opt. **42**, 257 (1995).

[5] D. W. Pohl, W. Denk, and M. Lanz, Appl. Phys. Lett. **44**, 651 (1984).

[6] E. Betzig and J. K. Trautman, Science **257**, 189 (1992).

[7] *Near Field Optics*, edited by D.W. Pohl and D. Courjon (Kluwer, Dordrecht, 1993).

[8] For recent developments in near-field optics, see Ultramicroscopy **57** (2/3) (1995).

[9] R. Reddick, R. Warmack, and T. Ferrell, Phys. Rev. B **39**, 767 (1989).

[10] L. Rayleigh, Philos. Mag. S **8**, 261 (1879).

[11] D. Courjon, J.-M. Vigourneux, M. Spajer, K. Sarayeddine, and S. Leblanc, Appl. Opt. **29**, 3734 (1990).

[12] N. Cerre, F. De Fornel, and J. P. Goudonnet, Appl. Opt. **31**, 903 (1992).

[13] S. Bozhevolnyi, M. Xiao, and O. Keller, Appl. Opt. **33**, 876 (1994).

[14] S. Bozhevolnyi, M. Xiao, and O. Keller (unpublished).

[15] A. Jalocha and N. F. van Hulst, Opt. Commun. **119**, 17 (1995).

[16] G. Krausch, S. Wegscheider, A. Kirsch, H. Bielefeldt, J. C. Meiners, and J. Mlynek, Opt. Commun. **119**, 283 (1995).

[17] S. Bozhevolnyi, I. Smolyaninov, and O. Keller, Appl. Opt. **34**, 3796 (1995).

[18] M. Specht, J. D. Pedarnig, W. M. Heckl, and T. W. Hänsch, Phys. Rev. Lett. **68**, 476 (1992).

[19] U. Ch. Fischer and D. W. Pohl, Phys. Rev. Lett. **62**, 458 (1989).

[20] O. Marti, H. Bielefeldt, B. Hecht, S. Herminghaus, P. Leiderer, and J. Mlynek, Opt. Commun. **96**, 225 (1993).

[21] P. Dawson, F. de Fornel, and J. P. Goudonnet, Phys. Rev. Lett. **72**, 2927 (1994).

[22] S. Bozhevolnyi, B. Vohnsen, I. Smolyaninov, and A. Zayats, Opt. Commun. **117**, 417 (1995).

[23] S. Bozhevolnyi, I. Smolyaninov, and A. Zayats, Phys. Rev. B **51**, 17 916 (1995).

[24] D. Tsai, J. Kovacs, Z. Wang, M. Moskovits, V. Shalaev, and J. Suh, Phys. Rev. Lett. **72**, 4149 (1994).

[25] J. R. Krenn, W. Gotschy, D. Somitsch, A. Leitner, and F. R. Aussenegg, Appl. Phys. A **61**, 541 (1995).

[26] F. Pincemin, A. Sentenac, and J. J. Greffet, Opt. Commun. **114**, 13 (1995).

[27] D. Maystre and M. Sailard, J. Opt. Soc. Am. A **11**, 680 (1994).

[28] J. C. Dainty, in *International Trends in Optics*, edited by J. W. Goodman (Academic, New York, 1991).

[29] A. R. McGurn, A. A. Maratudin, and V. Celli, Phys. Rev. B **31**, 4866 (1985).

[30] A. A. Maradudin, A. R. McGurn, and E. R. Méndez, J. Opt. Soc. Am. A **12**, 2500 (1995).
[31] P. W. Anderson, Philos. Mag. B **53**, 505 (1985).
[32] O. Keller, M. Xiao, and S. Bozhevolnyi, Surf. Sci. **280**, 217 (1993).
[33] M. Xiao, S. Bozhevolnyi, and O. Keller, Appl. Phys. A **62**, 115 (1996).
[34] M. Xiao and S. Bozhevolnyi, Opt. Commun. **130**, 337 (1996).
[35] C. Girard, Phys. Rev. B **42**, 9340 (1990); C. Girard and M. Spajer, Appl. Opt. **29**, 3726 (1990); C. Girard, *ibid.* **31**, 5380 (1992).
[36] M. Xiao, Opt. Commun. **132**, 403 (1996).
[37] M. Xiao, Chem. Phys. Lett. **258**, 363 (1996).
[38] M. Xiao, J. Mod. Opt. (to be published).
[39] O. Keller, Phys. Rev. B **37**, 10 588 (1988).
[40] O. Keller, M. Xiao, and S. Bozhevolnyi, Opt. Commun. **114**, 491 (1995).
[41] O. Keller, M. Xiao, and S. Bozhevolnyi, Opt. Commun. **102**, 238 (1993).
[42] O. Keller, S. Bozhevolnyi, and M. Xiao, in *Near Field Optics*, edited by D. W. Pohl and D. Courjon (Kluwer, Dordrecht, 1993), pp. 229–237.
[43] L. Mandel and E. Wolf, *Optical Coherence and Quantum Optics* (Cambridge University Press, New York, 1995).
[44] P. B. Johnson and R. W. Christy, Phys. Rev. B **6**, 4370 (1972).
[45] S. Bozhevolnyi, O. Keller, and M. Xiao, Appl. Opt. **32**, 4864 (1993).